CAMBRIDGE
UNIVERSITY PRESS

Article

Formation of iron-rich phyllosilicates in the FeO–SiO$_2$–H$_2$O system during hydrothermal synthesis as a function of pH

Liva Dzene[1] (ID), Amira Doggaz[1], Patrick Dutournié[1], Sayako Inoué[2] (ID), Mustapha Abdelmoula[3] (ID),

Alexandra Jourdain[1] (ID), Jean-Marc Le Meins[1], Jocelyne Brendlé[1], Christelle Martin[4] and Nicolas Michau[4] (ID)

[1]Institut de Science des Matériaux de Mulhouse CNRS UMR 7361, Université de Haute-Alsace, Université de Strasbourg, Mulhouse, France; [2]Geodynamics Research Center (GRC), Ehime University, Matsuyama, Ehime, Japan; [3]LCPME, CNRS-Université de Lorraine UMR7564, Nancy, France and [4]Andra, Scientific & Technical Division, Waste, Radionuclides, Chemicals & Geochemistry Department, Châtenay-Malabry, France

Abstract

The formation of iron-rich phyllosilicates can occur at different natural or engineered settings. In this study, the influence of pH in the hydrothermal synthesis of iron-rich phyllosilicates was investigated in the pH range 8.50–12.10 after the ageing of the precursor. The synthesized samples were characterized by powder X-ray diffraction, Raman and Mössbauer spectroscopies and transmission electron microscopy. Three domains of pH were identified, and these correlated with silica availability and its speciation in the solution. The formation of 1:1-type Fe^{III}/Fe^{II} phyllosilicate was observed between pH 9.67 and 10.75. Above pH 10.75, two types of phyllosilicate-like mineral phases were observed. In addition to 1:1-type Fe^{III}/Fe^{II} phyllosilicate, 2:1-type Fe^{III}/Fe^{II} phyllosilicate was observed. Below pH 9.67, mainly amorphous silica and iron oxides were observed. The findings show that pH governed the crystallinity and nature of the obtained phyllosilicate-like phases.

The damage to materials due to corrosion or scale formation can occur in engineered systems, especially when silicon and iron species are present in aqueous solution. Such conditions might occur in fluid-conducting pipes in brine-handling equipment and on glass–steel–cement interfaces in the context of a nuclear waste repository. In hyper-saline brines, the solution is basic, and high concentrations of silica and iron can occur, leading to the precipitation of Fe-rich phyllosilicates (Manceau, 1995). The scale formation can then clog pipes and damage other equipment. In the context of a nuclear waste repository, the pH of the cement material surrounding the steel containers is basic. As a result, some dissolved silica is expected to be present if the material is wet and porous. When in contact with metal where some Fe(II) could be leached, the formation of phyllosilicates can then be promoted, leading to further corrosion of steel (Lanson *et al.*, 2012; Herbert *et al.*, 2016). Si-OH species are present on the glass surface of the vitrified nuclear waste in significant amounts. When in contact with steel and dissolved Fe(II), phyllosilicate precipitation can thus be expected due to the high Si:Fe ratio, as shown in the studies of Carriere *et al.* (2021) and Galai *et al.* (2023) that identified phyllosilicate phases at the glass–steel interface. Silica consumption can induce glass alteration and, in some cases, accelerate the degradation of materials. The environmental conditions (element aqueous concentrations, pH, redox potential) of the formation of iron-rich layered phyllosilicates in the

FeO–SiO$_2$–H$_2$O system are poorly understood. Therefore, laboratory synthesis of such systems could provide new insights in this field.

The synthesis of iron-rich phyllosilicates using different protocols have been well documented (Petit *et al.*, 2017; Dzene *et al.*, 2018). The hydrothermal path remains the preferred one because of its versatility and ease of use, enabling relatively well-crystallized products to be obtained (Kloprogge, 1998; Jaber *et al.*, 2013). Many of the parameters that influence the synthesis products, such as synthesis time and temperature, chemical composition and pH, have been studied (Kloprogge, 1994; Lantenois *et al.*, 2005; Tosca *et al.*, 2016; Boumaiza *et al.*, 2020). For example, the preparation of precursors using Fe^{2+} could enhance the synthesis kinetics and crystallinity of the products (Decarreau & Bonnin, 1986). In general, it was also reported that low temperatures (<150°C) and short synthesis times favour the formation of Fe-serpentines (1:1-type phyllosilicate), whereas higher temperatures (>200°C) and longer synthesis times lead to the formation of Fe-rich saponite or chlorite (2:1-type phyllosilicate; Grubb, 1971; Bertoldi *et al.*, 2005; Mosser-Ruck *et al.*, 2010; Pignatelli *et al.*, 2014; Boumaiza *et al.*, 2020).

Amongst the synthesis parameters listed above, it has been demonstrated that pH had the greatest impact on the nature of the phases formed (Cundy & Cox, 2005; Baron *et al.*, 2016; Tosca *et al.*, 2016; Boumaiza *et al.*, 2020). Indeed, the quantity of hydroxyl anions (OH$^-$) in solution determines the speciation of elements and the solubility of reactants and products. Regarding the speciation of elements as a function of pH, Frank-Kamenetzkij *et al.* (1973) concluded in their study that for the mineral transformations that undergo dissolution and

precipitation, the pH of the medium controls the speciation of Al and thus the coordination of Al (octahedral *vs* tetrahedral) in newly formed structures. In an earlier study, de Kimpe *et al.* (1961) reported the formation of zeolite (where Al is tetrahedrally coordinated) under basic pH conditions and kaolinite (where Al is octahedrally coordinated) under acidic pH conditions. In addition, the recent study of Criouet *et al.* (2023) demonstrated the influence of the amount of OH^- on the synthesis of clay minerals. For the same chemical composition of the reactants, kaolinite was obtained in solutions at pH < 12, beidellite (with both octahedrally and tetrahedrally coordinated Al) was obtained in a solution at pH = 12 and zeolites (with only tetrahedrally coordinated Al) were formed in solutions at pH > 12. Under alkaline pH conditions, it has also been shown that the crystal chemistry of Fe(III)-nontronites is significantly controlled by aqueous Si speciation, which is pH dependent (Baron *et al.*, 2016). An increase in the proportion of $H_2SiO_4^{2-}{}_{(aq)}$ over $H_3SiO_4^-{}_{(aq)}$ was shown to enhance the Fe(III)–Si substitution in the obtained nontronites.

Regarding the $FeO–SiO_2–H_2O$ system, Francisco *et al.* (2020) demonstrated that polymerization of $Fe(OH)_2$ occurred under basic pH conditions, whereas the precipitation of amorphous SiO_2 was observed at pH < 8, inhibiting the polymerization of $Fe(OH)_2$. In addition, the studies of Schwertmann & Thalmann (1976) and Doelsch *et al.* (2002) demonstrated the formation of Si–O–Fe(II) bonds under basic pH conditions, hindering the polymerization of Fe(II) compounds. Halevy *et al.* (2017) observed the formation of green rust-like compounds at neutral pH, and the formation of iron-rich phyllosilicate (greenalite-like) phases under basic pH conditions was observed in the presence of silica (Konhauser *et al.*, 2007; Tosca *et al.*, 2016; Hinz *et al.*, 2021).

In our previous study, we observed that for the same targeted chemical composition, a great amount of hydroxyl ions available in the solution favoured the precipitation of 2:1-type phyllosilicate with respect to 1:1-type phyllosilicate, whereas a small quantity of OH^- favoured the formation of 1:1-type phyllosilicate (Boumaiza *et al.*, 2020). Given the strong dependence of the type of clay mineral obtained on pH and the pH dependence of silicon and iron species and/or compound speciation and solubility, the aim of this work was to go a step further and investigate whether a specific pH value can be found for the precipitation of 1:1-type iron-rich phyllosilicate in the $FeO–SiO_2–H_2O$ system. As mentioned above, the environmental conditions of the formation of iron-rich layered phyllosilicates, particularly those of 1:1-type phyllosilicates, in the $FeO–SiO_2–H_2O$ system are not well-known. The lack of such knowledge prevents us from reducing the degradation of materials and from increasing the durability of engineered systems where the formation of such phases can occur. An improved understanding of the formation mechanisms of these phases would allow us to prevent their formation in engineered systems. In cases in which such precipitation cannot be prevented, knowledge of the precipitation reactions and mechanisms could allow us to predict the evolution of such systems over large time scales.

Materials and methods

Chemicals

The following chemicals were used in this study: iron(II) sulfate heptahydrate ($FeSO_4{\cdot}7H_2O$, Sigma Aldrich, 99.90 wt.%) as the Fe(II) source, fumed silica (SiO_2, Aerosil® 380, Evonik) as the silicon source, powder sodium hydroxide (NaOH, Sigma Aldrich, 97 wt.%) to provide an alkaline medium and sodium dithionite

($Na_2S_2O_4$, Alfa-Aesar, 85 wt.%,) to maintain the reducing conditions. Deionized water (DIW; 18.2 MΩ·cm) was used for all of the experiments.

Synthesis protocol

The protocol is based on a hydrothermal synthesis starting from a suspension with an Fe:Si molar ratio of 1.5. Such a molar ratio would correspond to a theoretical structure $Si_2Fe_3O_5(OH)_4$ of greenalite and also be analogous to natural Mg-rich 1:1-type phyllosilicates. The procedure consisted of dissolving successively in 70 mL of DIW 0.041 g of $Na_2S_2O_4$, 4.510 g of $FeSO_4{\cdot}7H_2O$ ($[Fe^{2+}] = 0.232$ mol L^{-1}), 0.647 g of SiO_2 ($[Si] = 0.154$ mol L^{-1}) and a given quantity of NaOH ($[OH^-] = 0.45$–0.55 mol L^{-1}) to obtain a given pH (Table S1). Sodium dithionite was added to maintain the reducing conditions, as mentioned in previous synthesis protocols of similar materials (Harder, 1978; Mizutani *et al.*, 1991). The given amount of NaOH was added to vary the pH. The range of this amount was determined based on our previous study (Boumaiza *et al.*, 2020), in which the formation of 1:1-type phyllosilicate was observed with an OH:Fe molar ratio of 2.4. Note that for some experiments the OH:Fe molar ratio was the same but the measured pH values were slightly different. In practice, it was the obtained pH value that determined the synthesis outcome, as demonstrated further by the results. The mixture was stirred over 2 h at room temperature before being sealed in a Teflon-lined stainless-steel mineralization bomb (Top Industrie®, 150 mL) for 2 days at 160°C. The synthesis time and temperature were chosen based on our previous study (Boumaiza *et al.*, 2020). After the hydrothermal treatment, the bomb was cooled down until it reached room temperature. The product was recovered and washed three times with DIW by dispersion centrifugation at 8000 rpm for 5 min (9946 *g*) and dried at 60°C. The resulting product mass after washing was ∼1.8 g.

The pH of the aged suspensions after 2 h (pH_i) and of the solutions after the hydrothermal treatment (pH_f) were measured at 25°C using an Orion™ ThermoFisher electrode ($pH \pm 0.01$) calibrated with two buffer solutions at pH 7.0 and 10.0.

Characterization methods

Powder X-ray diffraction

Data were collected with a powder Bruker diffractometer D8 ADVANCE (Germany) in Bragg-Brentano reflexion geometry θ–θ (goniometer radius = 280 mm). This diffractometer was equipped with the LynxEye XE-T high-resolution energy-dispersive 1-D detector (Cu-$K\alpha_{1,2}$). This kind of detector allows us to avoid Fe fluorescence effects with Cu X-ray tubes. The X-ray diffraction (XRD) traces were recorded under the following conditions: angular area 3–70°2θ, step size 0.017°2θ, time per step 1.8 s (total time per step = 345 s), variable divergence slit mode (irradiated sample length = 15 mm) and total time for acquisition 2 h. During the data collection, powder samples were rotated at 5 rpm. A motorized anti-scatter screen was used for effective suppression of the instrument background, most importantly air scatter at low 2θ angles.

Raman spectroscopy

Raman spectra were obtained with a Horiba LABRAM 300 confocal Raman spectrometer (France) equipped with a Compass 315M-50 laser (50 mW, 632 nm), diffraction gratings of 600 grooves mm^{-1} and a charge-coupled device (CCD) matrix

detector. Laser focusing and sample viewing were performed through an Olympus BX40 microscope fitted with a ×50 objective lens. The spot size was ~15–20 μm and resolution was 4 cm^{-1}. Laser power could be reduced by filters to ~1.00, 0.10 and 0.01 mW.

Transmission electron microscopy

Powder samples were impregnated in epoxy resin (Bond E-set, Konishi Bond, Japan) and sandwiched between two glass slides to ensure the preferred orientation of the samples. The sandwiched samples were sliced and polished mechanically. The transmission electron microscopy (TEM) lamella (10.00 × 5.00 × ~0.15 μm) was prepared using the focused ion beam (FIB) lift-out technique in a dual beam FIB scanning electron microscope (SEM; Thermo Fisher Scientific Scios and Scios2, USA). The specimens prepared using the FIB were characterized using a field-emission TEM (FE-TEM; JEOL JEM-2100F HR, Japan) operated at 200 kV. High-resolution TEM (HRTEM) images were recorded using a Gatan Ultrascan 100XP bottom-mounted CCD camera (USA). Some of the HRTEM images were processed using the Wiener filter (Marks, 1996; Kilaas, 1998) developed by K. Ishizuka (HREM Research, Inc., Japan), which was implemented in *Gatan Digital Micrograph* software (USA) to remove noise contrast. Energy-dispersive X-ray spectroscopy (EDS) imaging was performed using a JEOL JED-2300T silicon drift detector equipped on the TEM in scanning TEM mode.

Mössbauer spectroscopy

A Mössbauer spectrometer was equipped with a 512 multichannel analyser (Halder Electronic Gmbh, Germany) and a 50 mCi source of ^{57}Co in the Rh matrix. Mössbauer analysis was performed at 290 and 12 K with constant acceleration. Data were obtained from appropriate amounts (10 mg of Fe per cm^2) of solid samples to achieve optimal experimental conditions. To avoid the condensation of oxygen and water on the walls of the cryostat, samples were quickly transferred under an inert He atmosphere to a cold-head cryostat equipped with a vibration isolation stand and developed in the LCPME Laboratory (France). The recordings at 290 K were performed on the spectrometer equipped with the Advanced Research Systems cryostat, whereas the recordings at 12 K were performed on the spectrometer coupled to the Janis Cryostat. Mössbauer spectra were collected in transmission mode. The 50 mCi source of ^{57}Co in the Rh matrix was maintained at room temperature and mounted at the end of a Mössbauer velocity transducer. The spectrometer was calibrated with a 25 μm foil of α-Fe at room temperature. Analysis of the Mössbauer spectra consisted of least-square fitting of the data with a combination of two-peak quadrupole components (doublets) and, when present, six-peak magnetic hyperfine components (sextets). Computer fitting with Lorentzian shape lines is usually sufficient to fit such spectra. However, the Voigt profile analysis of Rancourt & Ping (1991) for quadrupole splitting distribution and magnetic hyperfine fields can be more relevant for analyses of dynamic effects on spectral line broadening.

Calculation of theoretical solubility and speciation of silicon compounds

Table 1 summarizes the equations used to calculate the theoretical solubility and speciation of silicates corresponding to the experimental conditions used during the preparation of the precursors at room temperature.

Table 1. Theoretical concentration (C) and speciation of amorphous silica in water at 298 K.

$C < C_0 = 0.154$ mol L^{-1}	$C = C_0 = 0.154$ mol L^{-1}
$\boldsymbol{C} = [\mathrm{H_4SiO_4}] + [\mathrm{H_3SiO_4^-}] + [\mathrm{H_2SiO_4^{2-}}]$	
$\boldsymbol{C} = 10^{-2.7}\left(1 + \frac{10^{-9.7}}{10^{-\mathrm{pH}}}\left(1 + \frac{10^{-13.2}}{10^{-\mathrm{pH}}}\right)\right)$	$C = C_0$
$[\mathrm{H_4SiO_4}] = 10^{-2.7}$	$[\mathrm{H_4SiO_4}] = \left[\left(\frac{C_0}{1 + \frac{10^{-9.7}}{10^{-\mathrm{pH}}}\left(1 + \frac{10^{-13.2}}{10^{-\mathrm{pH}}}\right)}\right)\right]$
$[\mathrm{H_3SiO_4^-}] = 10^{-2.7}\left[\left(\frac{1 + \frac{10^{-9.7}}{10^{-\mathrm{pH}}}\left(1 + \frac{10^{-13.2}}{10^{-\mathrm{pH}}}\right)}{\frac{10^{-\mathrm{pH}}}{10^{-9.7}} + 1 + \frac{10^{-13.2}}{10^{-\mathrm{pH}}}}\right)\right]$	$[\mathrm{H_3SiO_4^-}] = \left[\left(\frac{C_0}{\frac{10^{-\mathrm{pH}}}{10^{-9.7}} + 1 + \frac{10^{-13.2}}{10^{-\mathrm{pH}}}}\right)\right]$
$[\mathrm{H_2SiO_4^{2-}}] = 10^{-2.7}\left[\left(\frac{1 + \frac{10^{-9.7}}{10^{-\mathrm{pH}}}\left(1 + \frac{10^{-13.2}}{10^{-\mathrm{pH}}}\right)}{1 + \frac{10^{-\mathrm{pH}}}{10^{-13.2}}\left(1 + \frac{10^{-\mathrm{pH}}}{10^{-9.7}}\right)}\right)\right]$	$[\mathrm{H_2SiO_4^{2-}}] = \left[\left(\frac{C_0}{1 + \frac{10^{-\mathrm{pH}}}{10^{-13.2}}\left(1 + \frac{10^{-\mathrm{pH}}}{10^{-9.7}}\right)}\right)\right]$

$[\mathrm{H_4SiO_4}] = 10^{-2.7}$ mol kg^{-1} H$_2$O (solubility constant of amorphous silica is $10^{-2.7}$ at 298 K; Gunnarsson & Arnórsson, 2000); pKa (H$_3$SiO$_4^-$/H$_4$SiO$_4$) = 9.7 (Alexander *et al.*, 1954); pKa (H$_2$SiO$_4^{2-}$/ H$_3$SiO$_4^-$) = 13.2 (Eikenberg, 1990); C_0 = [Si]$_{\mathrm{initial}}$ = 0.154 mol L^{-1}.

In this study, we chose a simple model of silica speciation even though a more realistic speciation of silica species, especially at pH > 10, has been proposed (Felmy *et al.*, 2001). The suggested model considers dimeric, trimeric (linear, cyclic and substituted), tetrameric (linear and cyclic) and hexameric (prismatic) species in addition to monomeric ones. However, the monomeric species remain the major species in solution and could therefore be considered as a good first approximation.

Measurements of electrolytic conductivity

The conductimetry experiments were conducted with a conductimeter PC 5000 L Phenomenal (VWR, PA, USA). The ionic conductivity of the solution was assumed to be the sum of the specific conductivity of each ion in solution. Each chemical contribution was investigated by measuring the conductimetry of the solution as a function of the amount of added OH$^-$. Two experiments were performed: (1) addition of a given amount of 1 M NaOH solution in DIW; and (2) addition of a given amount of 1 M NaOH solution in DIW containing 0.647 g of fumed silica (SiO$_2$, Aerosil® 380, Evonik).

Results

Mineralogical composition of the synthesis products: identification of three domains

The XRD powder analysis of the products revealed three distinct domains that differed according to the nature of phyllosilicates obtained (Fig. 1). For lower OH:Fe ratios (<2.10) corresponding to pH$_i$ < 9.67, the XRD traces showed the presence of some broad yet characteristic peaks of *hkℓ* reflections of phyllosilicates, but the peaks of *00ℓ* reflections were not observable. For higher OH:Fe molar ratios (2.10–2.16) corresponding to pH$_i$ = 9.67–10.75, the 1:1-type phyllosilicate could be identified by its characteristic peak at 7 Å. At higher OH:Fe ratios (>2.16) leading to pH$_i$ that exceeded 10.75, both 1:1- and 2:1-type phyllosilicates were identified in the synthesis products, characterized by the peaks at 7 and 12 Å, respectively. It must be noted that all of the synthetized products contained iron oxide and/or hydroxide phases. Some of the samples contained thenardite (Na$_2$SO$_4$), which formed from the sulfate anions and sodium cations and had remained due to incomplete washing. A more detailed characterization of three samples representing each domain was carried out by powder XRD analysis, Raman and Mössbauer spectroscopies and TEM.
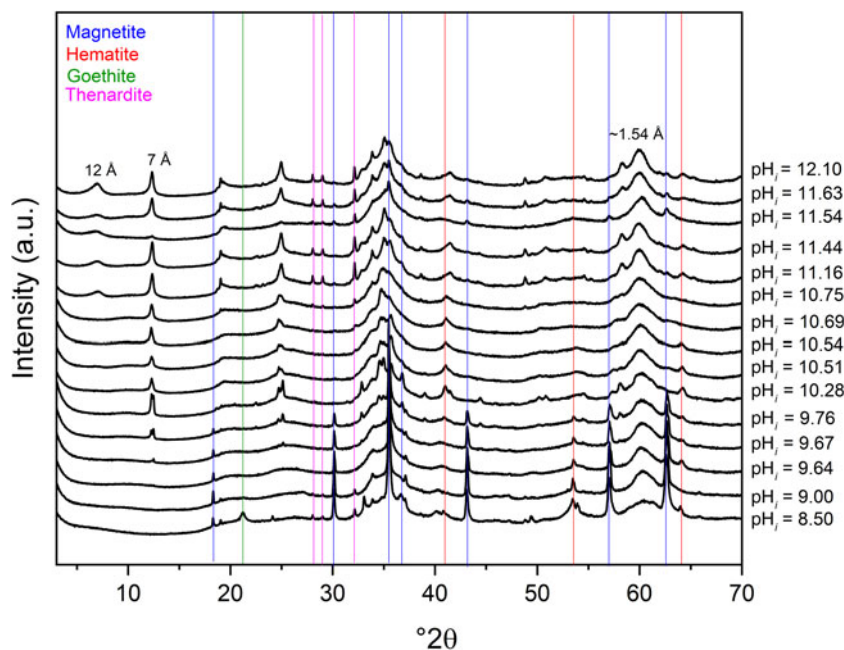
Figure 1. Powder XRD traces of the synthesis products obtained by varying the initial OH:Fe molar ratio from 1.93 to 2.39 (pH$_i$ = 8.50–12.10).

Characterization of synthesis products in domain 1 where pH$_i$ < 9.67

A sample prepared with a pH$_i$ value of 8.50, representing domain 1, was chosen for a more detailed characterization. The powder XRD trace revealed reflections at 4.84 Å (18.28°2θ), 2.78 Å (32.17°2θ) and 2.09 Å (43.14°2θ), corresponding to magnetite (Fig. 2a). The characteristic reflections of hematite at 2.69 Å (33.15°2θ) and at 1.45 Å (64.02°2θ) and of goethite at 4.17 Å (21.28°2θ) were also identified. Broad peaks corresponding to the diffraction angles of phyllosilicate planes at 2.57 Å (34.32°2θ) and at 1.52 Å (60.37°2θ) suggested the formation of a poorly crystalline phyllosilicate phase (Stucki *et al.*, 1989). The high signal intensity above the baseline suggested the presence of amorphous compounds in the sample, such as amorphous silica.

Raman spectroscopy confirmed the presence of magnetite with characteristic bands at 302 and 668 cm^{-1} (Fig. 2b; de Faria *et al.*, 1997). The hematite and goethite phases could not be detected probably due to their low amounts in the sample.

A highly crystalline clay structure was not observed in the TEM images. Only a low-crystalline phase with a sheet-like texture was seen (Fig. 2c). The selected area electron diffraction (SAED) pattern gave a halo ring pattern characteristic for a low-crystalline phase (Fig. S1). No significant changes in the SAED pattern and HRTEM image were observed during the continuous illumination of the electron beam. Moreover, Ga contamination by the FIB was negligible in the analysed area. These results indicate that the low-crystalline phase was not formed due to beam damage during the specimen preparation process by FIB nor by TEM observation. The chemical analysis of this area yielded molar Fe:Si = 0.73, suggesting that this low-crystalline phase could correspond to a 2:1-type phyllosilicate-like structure. This observation agrees with the XRD results (Fig. 2a), where no 001 reflection peak, characteristic for phyllosilicates, was observed, and where only broad reflections at ~35°2θ and 60°2θ (corresponding to 2.6 and 1.53 Å, respectively) were recorded. The absence of 00ℓ reflections in the XRD traces indicates that the stacking of layers is absent. Indeed, the TEM observation revealed

a phase with a sheet-like texture but small size and only a few layers thick.

The deconvolution of the Mössbauer spectrum acquired at room temperature confirmed the presence of various iron-bearing phases: magnetite, goethite and iron-rich phyllosilicate (Fig. S2 & Table S2). These results were in agreement with the mineralogical composition identified in the powder XRD traces. The phyllosilicate phase contained two Fe(III) components, which could be attributed to both the octahedral and tetrahedral sites (Dyar *et al.*, 2006). The spectrum recorded at low temperature (Fig. 2d) confirmed the nature of the observed phases at room temperature (Fig. S2). The iron oxide components' contribution to the recorded signal was more significant, as expected, at low temperature (Table 2). The sextet characterized by the magnetic field of 487 kOe and negative quadrupole shift ε (–0.28 mm s^{-1}) was attributed to goethite (Murad & Johnston, 1987; Benali *et al.*, 2001), whereas the five other sextets can be assigned to magnetite as previously established for this mineral at very low temperatures in the literature (Vandenberghe *et al.*, 2000; Meite *et al.*, 2022).

Considering the obtained EDS chemical analysis (Table 3) and iron oxidation state obtained from Mössbauer spectroscopy at 12 K, the formula of the phyllosilicate in domain 1 could be estimated as Fe$_{2.16}^{III}$(Si$_{3.51}$Fe$_{0.49}^{III}$)O$_{10}$(OH)$_2$, corresponding to a 2:1-type phyllosilicate-like phase. It should be noted that more detailed tests such as cation-exchange experiments would allow to establish a more realistic formula. However, for such experiments a pure phase would be needed, which is not the case here. Nevertheless, the characterizations performed in this study allow us to suggest a first approximate estimation of the obtained phase. In summary, the samples obtained in this domain contained magnetite, goethite and a poorly crystalline 2:1-type Fe(III)-rich phyllosilicate-like phase.

Characterization of synthesis products in domain 2 with 9.67 ≤ pH$_i$ ≤ 10.75

For domain 2, a sample with pH$_i$ = 10.28 was chosen for more detailed characterization. The XRD traces revealed the presence
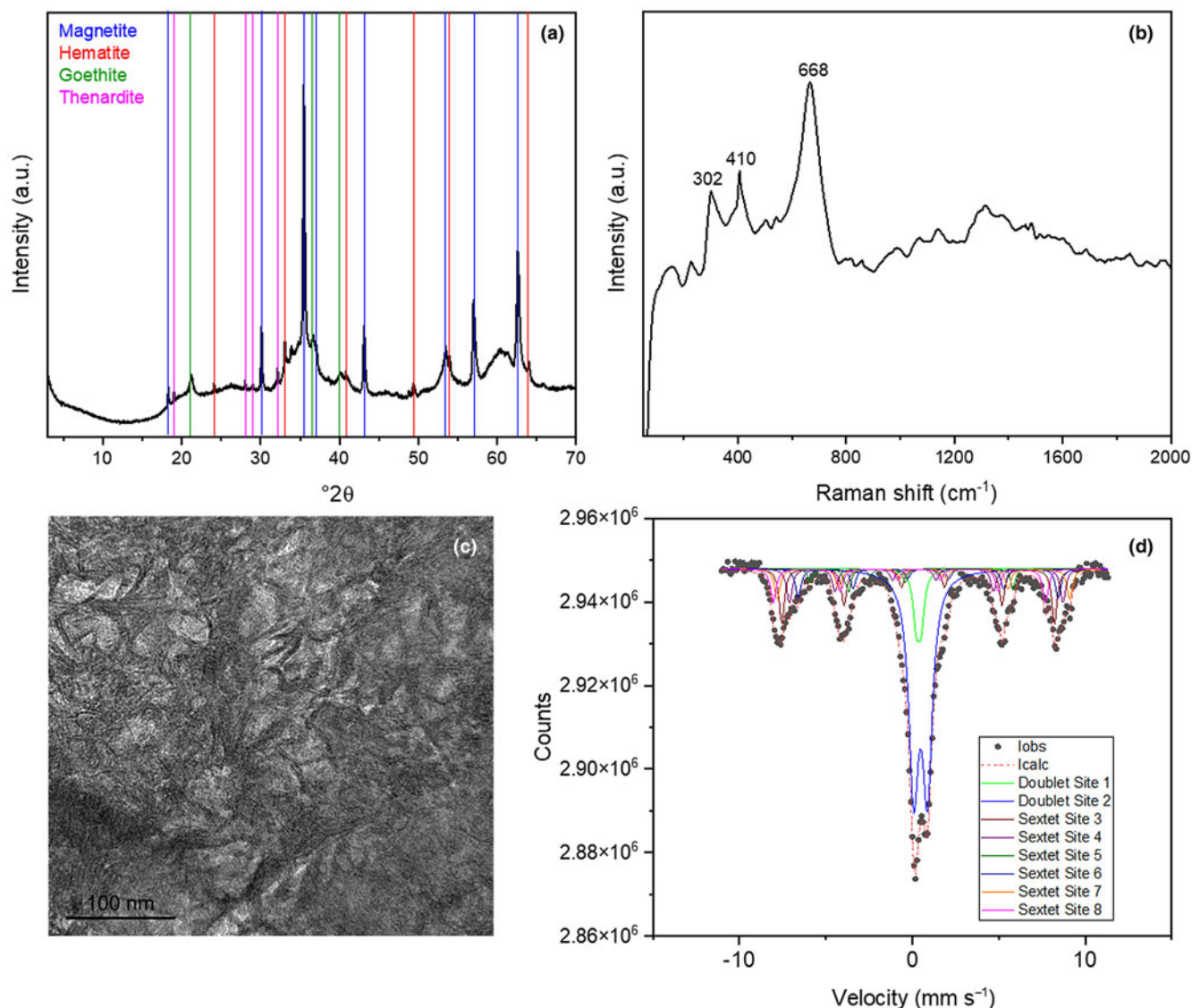
Figure 2. (a) XRD trace, (b) Raman spectrum, (c) TEM image and (d) Mössbauer spectrum at 12 K of a sample with $pH_i = 8.50$.

of a phyllosilicate of 1:1 type with its main peak at 7 Å (12.44°2θ) and other peaks at 3.56 Å (25.01°2θ) and 1.53 Å (60.40°2θ; Fig. 3a). A broad peak at ~10°2θ suggested possibly a second poorly ordered 1:1-type phyllosilicate phase. Peaks of hematite

were also detected at 1.45 Å (64.22°2θ) and 1.69 Å (54.49°2θ). Raman data confirmed the presence of hematite with characteristic intensive bands at 223, 293, 410, 507, 610 and 1321 cm^{-1} (Fig. 3b; de Faria *et al.*, 1997). Observation in TEM revealed a layered structure characteristic of a 1:1-type phyllosilicate with an average basal spacing of 7 Å (Fig. 3c). The SAED pattern confirmed a periodicity of 7 Å (Fig. S3). The chemical analysis of the area yielded a molar Fe:Si ratio of 1.71 (the initial ratio was 1.50).

The Mössbauer spectrum at room temperature revealed two components corresponding to Fe(III) and Fe(II) in a phyllosilicate structure (Fig. S4 & Table S3). The spectrum at low temperature also revealed the presence of an iron oxide phase (hematite; Fig. 3d & Table 4).

Considering the obtained EDS chemical analysis (Table 3) and iron oxidation state obtained from Mössbauer spectroscopy at 13 K, the formula of phyllosilicate in domain 2 could be estimated as $Fe^{II}_{0.39}Fe^{III}_{1.96}(Si_{1.35}Fe^{III}_{0.65})O_5(OH)_4$, corresponding to a serpentine-like structure. Although the tetrahedrally coordinated Fe^{3+} was not suggested by the Mössbauer spectroscopy, it is reasonable to assume that there is no vacant site in the tetrahedral sites.

Table 2. Mössbauer parameters for the synthesis products with $pH_i = 8.50$ at 12 K.

	CS (mm s^{-1})	Δ (mm s^{-1})	H (kOe)	RA (%)	
Doublet (1)	0.36	0.27	–	6	Fe(III) in phyllosilicate
Doublet (2)	0.48	0.76	–	45	Fe(III) octahedral in phyllosilicate
Sextets	0.48	−0.139	488	12	Magnetite
	0.44	0.36	490	8	
	1.04	2.11	294	5	
	0.93	0.05	465	8	
	0.62	0.03	523	8	
Sextet	0.32	−0.28	487	8	Goethite

Δ = quadrupole splitting; CS = centre shift; H = hyperfine field; RA = relative abundance.

Table 3. Chemical composition of the samples.

pH$_i$	8.50	10.28	11.63	
Type of structure	2:1	1:1	1:1	2:1
SiO$_2$	52.49	27.29	38.06	38.53
FeO^a	47.51	72.71	61.94	61.47
Total	100.00	100.00	100.00	100.00
Fe^{3+}/ΣFe by MS	1.00	0.87	0.88	0.88
O	11	7	7	11
Si	3.51	1.35	1.77	2.80
Fe^{3+}(IV)^b	0.49	0.65	0.23	1.20
ΣTetrahedral cations	4.00	2.00	2.00	4.00
Fe^{2+}	–	0.39	0.29	0.45
Fe^{3+}(VI)	2.16	1.96	1.88	2.10
ΣOctahedral cations	2.16	2.35	2.17	2.55
Number of octahedral vacancies	0.84	0.65	0.83	0.45

^{a}Total iron as FeO.
^{b}Tetrahedral Fe^{3+} was determined assuming that there is no tetrahedral vacancy.
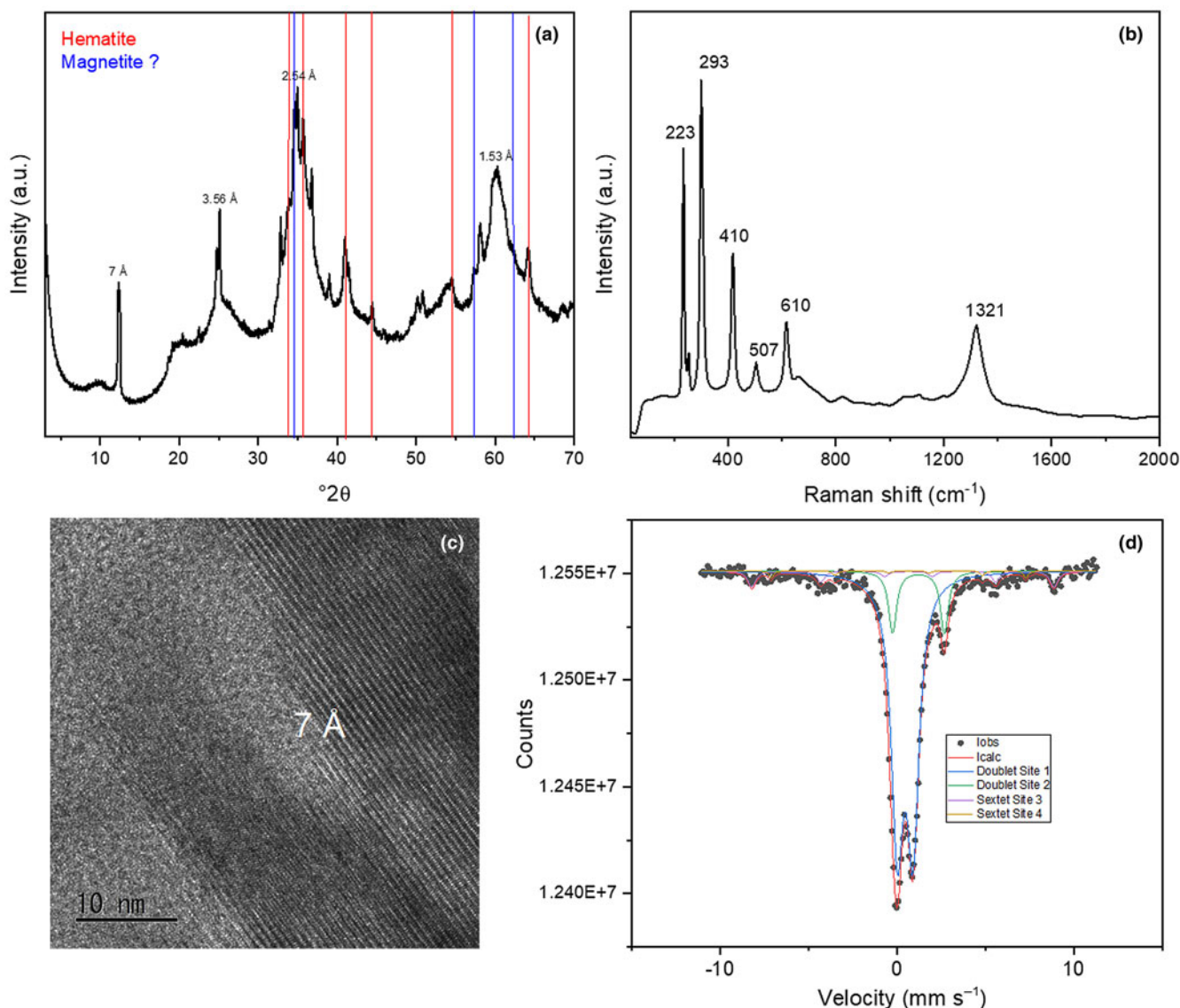MS = Mössbauer spectroscopy.

Therefore, some of the Fe^{3+} was assigned to the tetrahedral site. In summary, samples obtained in this domain were composed of hematite and a serpentine-like phyllosilicate.

Characterization of synthesis products in domain 3 with pH$_i$ > 10.75

The sample with pH$_i$ = 11.63 was studied in detail. The XRD data showed the presence of two types of phyllosilicates – a 2:1 type and a 1:1 type – identified by their characteristic peaks at 12 and 7 Å, respectively. Some broad reflections corresponding to iron oxides, magnetite and/or hematite were identified. The diffraction peaks at 4.65 Å (19.05°2θ), 3.17 Å (28.14°2θ) and 3.07 Å (29.04°2θ) corresponded to thenardite (Na$_2$SO$_4$), attributed to the use of sodium hydroxide and ferrous sulfate as precursors (Fig. 4a). The Raman spectrum corresponded to that of hematite, with the characteristic peaks as reported for domain 2 (Fig. 4b).

The observation of particles in TEM revealed a clay mineral-like phase with 7 Å periodicity (Fig. 4c). Low-crystallinity regions

Figure 3. (a) XRD trace, (b) Raman spectrum, (c) TEM image and (d) Mössbauer spectrum at 13 K (D) of the sample with pH$_i$ = 10.28.

Table 4. Mössbauer parameters for the synthesis product with pH_i = 10.28 at 13 K.

	CS (mm s^{-1})	Δ (mm s^{-1})	H (kOe)	RA (%)	
Doublet (1)	0.48	0.88	–	79	Fe(III) in phyllosilicate
Doublet (2)	1.23	2.92	–	12	Fe(II) in phyllosilicate
Sextet (3)	0.50	−0.15	529	7	Iron oxide (hematite)
Sextet (4)	0.39	−0.05	450	2	Iron oxide (hematite)

Δ = quadrupole splitting; CS = centre shift; H = hyperfine field; RA = relative abundance.

were also observed (Fig. S5) with a sheet-like texture. Indeed, the 2:1 phyllosilicate phase identified by XRD had broad peaks suggesting poor crystallinity, which is in agreement with the TEM observations (Fig. S5).

The Mössbauer spectrum obtained at room temperature could be deconvoluted into four components corresponding to two types of Fe(III) site and two types of Fe(II) site (Fig. S6 & Table S4). Considering the presence of 2:1- and 1:1-type phyllosilicates in the sample, at least some of the Fe(III) and Fe(II) sites observed on the room temperature spectrum belong to the phyllosilicate phase. The Mössbauer spectrum at low temperature differed significantly from the Mössbauer spectrum at room temperature. Additional magnetic components composed of three sextets (which were absent at room temperature) appeared in the low-temperature spectrum (Fig. 4d). As a consequence, the relative abundance of the paramagnetic components of Fe(III) decreased from 80% in the room temperature spectrum to only 21% in the low-temperature spectrum (Table 5). Such behaviour confirmed the presence of poorly crystalline iron oxides in the sample, as suspected from the broad peaks in the XRD trace and as evidenced by Raman spectroscopy or on the basis of the relaxation phenomena observed in magnetic structures obtained at low temperatures and due to the superparamagnetic behaviour of iron oxides as obtained by Meite *et al.* (2022). However, the phenomenon of super-paramagnetism, which is a good indication of the small size of the particles, as also suggested by XRD and TEM, may render such interpretation more difficult.

The chemical composition of phyllosilicate-like phases was estimated by TEM-EDS analyses of the 7 Å and poorly crystalline
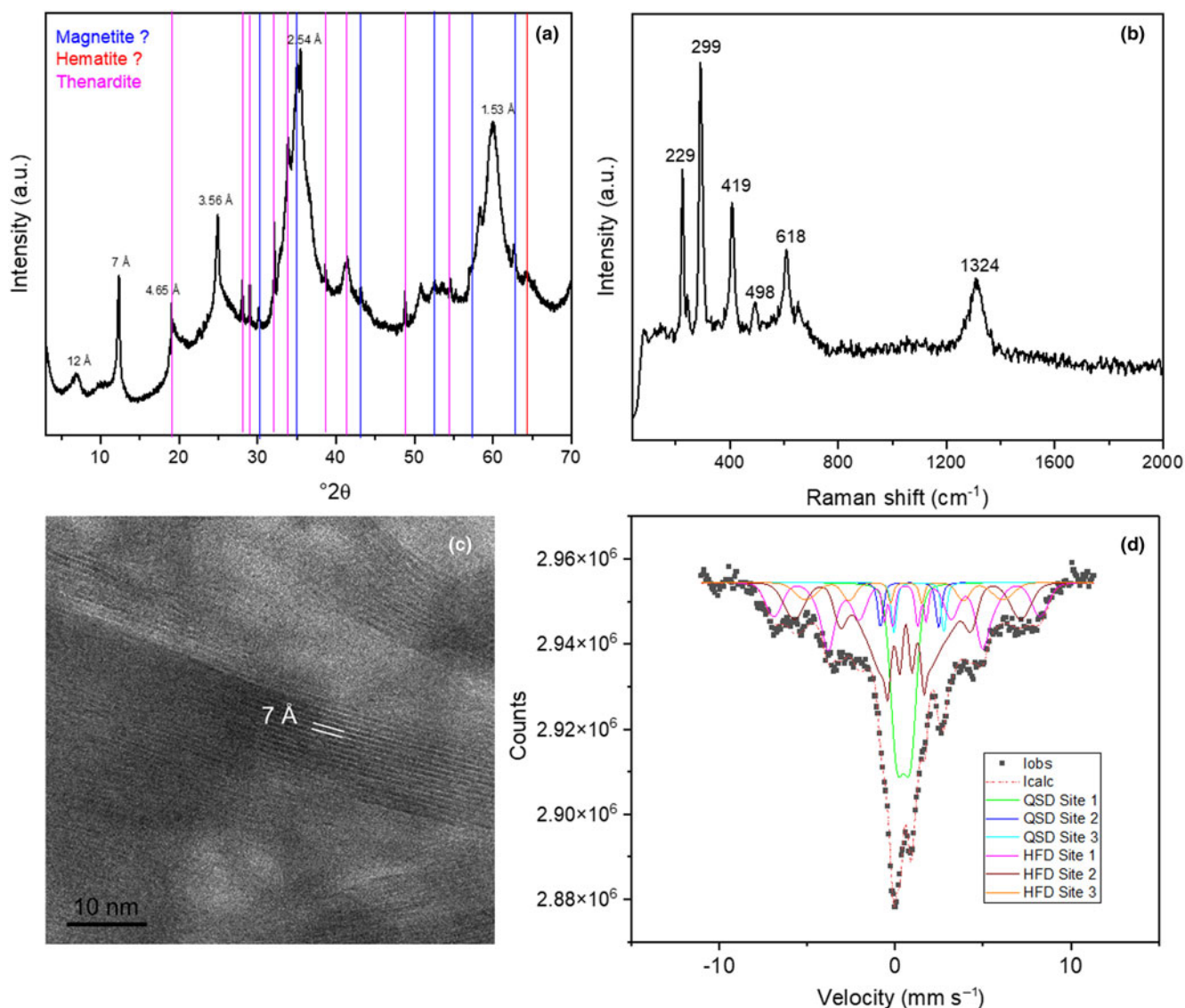
Figure 4. (a) XRD trace, (b) Raman spectrum, (c) TEM image and (d) Mössbauer spectrum at 11 K of the sample with pH_i = 11.63.

Table 5. Mössbauer parameters for the synthesis product with $pH_i = 11.63$ at 11 K.

|	CS (mm s^{-1})	Δ (mm s^{-1})	H (kOe)	RA (%)	
Doublet (1)	0.47	0.83	–	21	Fe(III) in phyllosilicate
Doublet (2)	0.82	3.3	–	3	Fe(II) in phyllosilicate
Doublet (3)	1.35	2.84	–	3	Fe(II) in phyllosilicate
Sextet (4)	0.62	0.05	360	25	Iron oxide
Sextet (5)	0.65	0.04	224	41	Iron oxide
Sextet (6)	0.57	−0.05	380	7	Iron oxide

Δ = quadrupole splitting; CS = centre shift; H = hyperfine field; RA = relative abundance.

regions of the particles (Table 3). In both cases, the molar Fe:Si ratio was between 1.32 and 1.36. Assuming that doublet (3) (Table 5) would correspond to a 1:1-type phyllosilicate phase and doublet (2) would correspond to a 2:1-type phyllosilicate-like phase, an estimation of the formula was attempted. For the 1:1-type phyllosilicate-like phase it gave $Fe_{0.29}^{II}Fe_{1.88}^{III}(Si_{1.77}Fe_{0.23}^{III})O_5(OH)_4$, corresponding to a serpentine-like phase similar to the one obtained for domain 2, and for the 2:1-type phyllosilicate-like phase it gave $Fe_{0.45}^{II}Fe_{2.10}^{III}(Si_{2.80}Fe_{1.20}^{III})O_{10}(OH)_2$, corresponding to the 2:1-type phyllosilicate-like phase. In summary, the samples obtained in this domain contained phyllosilicate-like phases of serpentine and 2:1 phyllosilicate type, and possibly hematite, which was detected by Raman and Mössbauer spectroscopies.

Evolution of pH: correlation with three domains of distinct mineralogical composition

The pH of the medium was measured after 2 h of the ageing of the precursor (pH_i) and after the hydrothermal treatment (pH_f). It should be noted that the pH after the addition of reactants (pH_0) in all samples was higher than the pH_i. Three domains were identified that differed between each other with respect to the evolution between pH_i and pH_f (Fig. 5). The identified domains here correlated with those identified with respect to the mineralogical composition in Fig. 1.

In the first domain where $pH_i \leq 9.67$, the final pH was lower compared to the pH_i. This suggested the consumption of OH$^-$
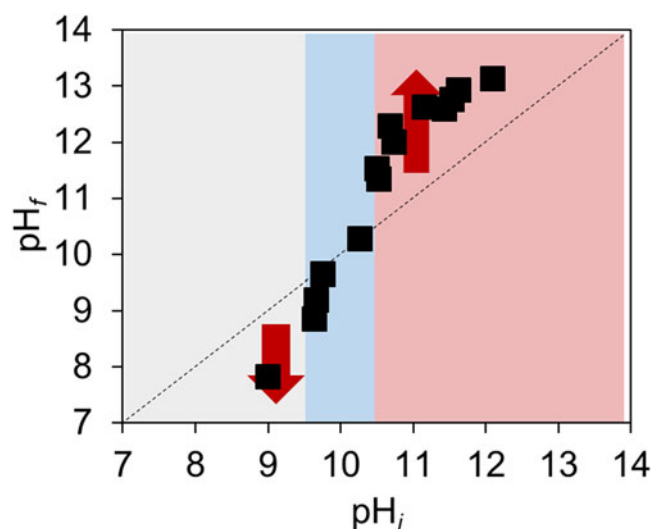
Figure 5. Comparison between pH after hydrothermal treatment (pH_f) and pH after ageing of precursor (pH_i).

and/or the production of H$^+$. These ions were used in the condensation reactions, resulting in the formation of iron oxides minerals: magnetite, hematite and goethite (Schwertmann & Cornell, 2000). These phases were identified by different characterization techniques (Fig. 2). In the second domain, where $9.60 < pH_i < 10.75$, the pH remained stable throughout the experiment and did not change after the hydrothermal treatment. During the precipitation reactions, the amount of consumed OH$^-$ was expected to be equal to the amount of the released OH$^-$. This domain corresponded to the precipitation of a 1:1-type phyllosilicate (Fig. 3). In the third domain, where $pH_i \geq 10.75$, the pH after the hydrothermal treatment increased with respect to the pH after the ageing of the precursor. This suggested the release of OH$^-$ as a result of reactions leading to the precipitation of both 1:1- and 2:1-type phyllosilicates (Fig. 4). It has to be noted that the overall amount of OH$^-$ in solution decreased with respect to the initially introduced amount. However, during the ageing of the precursor more OH$^-$ was consumed with respect to what is needed to phyllosilicate precipitation only. This can be explained by the consumption of OH$^-$ to solubilize silica and to associate with Fe(II) aqueous species. This quantity of initially consumed OH$^-$ was then partially released when the formation of phyllosilicates occurred.

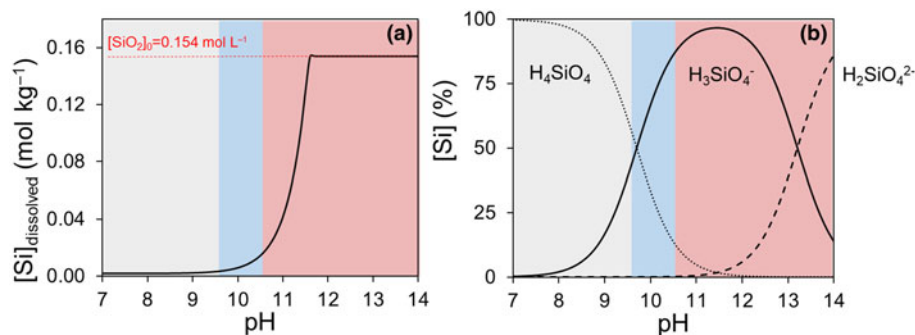### Theoretical solubility of silica compounds and speciation of dissolved silica species as a function of pH

According to the literature (Gunnarsson & Arnórsson, 2000), the solubility constant of amorphous silica is $10^{-2.7}$ at 298 K. The theoretical solubility for dissolved silica was calculated using the equations in Table 1, which is represented in Fig. 6a. It can be seen that when pH < 9.0 the amount of dissolved silica is very low, and when pH > 11.6 all of the initial amount of silica is dissolved.

In domain 1, the formation of iron oxyhydroxides was observed. The very low solubility of silica could explain the absence of well-crystallized phyllosilicates and the presence of residual amorphous silica. Indeed, an amorphous silica could be a precursor of iron-rich phyllosilicates (Francisco *et al.*, 2020). The increase in the solubility of silica correlated with the presence of crystalline phyllosilicate phases in synthesized samples observed in domains 2 and 3. The availability of dissolved silica species favoured the reactions leading to the precipitation of phyllosilicates.

Interestingly, the precipitation of the 1:1-type phyllosilicate was observed only at pH > 9.7. This could be related to the net increase in the solubility of amorphous silica above this value. However, in domain 1, the precipitation of 2:1-type phyllosilicate was identified. The formation of 2:1-type phyllosilicate requires more silicon compared to the formation of 1:1-type phyllosilicate. It should be noted that the precipitated 2:1-type phyllosilicate was poorly crystalline due to the small quantity of silica available. However, despite the low quantity of aqueous silica species available, 2:1type phyllosilicate was still formed, suggesting that the solubility of amorphous silica would determine only the crystallinity of the phyllosilicate formed and not its type.

The lower limit for the formation of 1:1-type phyllosilicate correlates with silica aqueous speciation (Fig. 6b). From pH 9.7 to 13.2, the main species in solution is trihydrogen orthosilicate ($H_3SiO_4^-$). Below pH 9.7, the predominant species is silicic acid (H_4SiO_4). Above pH 13.2, the dissolved silica is mainly in the form of dihydrogenorthosilicate ($H_2SiO_4^{2-}$). The coincidence of

Figure 6. (a) Theoretical solubility of amorphous silica and (b) speciation of silica aqueous species as a function of pH at 298 K.

the formation of 1:1-type phyllosilicate with the lower limit of predominance of $H_3SiO_4^-$ at pH = 9.7 suggests that the presence of this species in solution is necessary for the formation of 1:1-type phyllosilicate particles.

Experimental solubility of silica as a function of $[OH]_{introduced}^-$ determined by measuring electrolytic conductivity

Conductivity is proportional to the quantity of charged species in solution. Indeed, when the amount of OH^- ions is increased *via* the introduction of 1 M NaOH solution, a positive linear relationship with conductivity is found (filled dots in Fig. 7a). When the same experiment is repeated in the presence of amorphous silica (empty squares in Fig. 7a), a positive linear relationship with conductivity was also observed, but this relationship was less pronounced due to the consumption of OH^- used to dissolve SiO_2.

If we know the amount of OH^- consumed to dissolve SiO_2, the amount of $[Si]_{dissolved}$ can then be calculated (empty circles in Fig. 7b). The dissolved amount of Si thus obtained can be then compared to the theoretical solubility of silica as a function of pH (black line in Fig. 7b). The calculated amount of dissolved SiO_2 from conductivity measurements follows the same trend as the theoretical solubility of silica. The experimental amount of dissolved Si is probably overestimated between pH 10 and 11 due to significant uncertainties related to the pH measurements. Above pH 11, the calculated amount of dissolved SiO_2 from

conductivity measurements increases similarly to the theoretically predicted amount. The difference between the experimentally dissolved silica and theoretically predicted quantity should be due to the dissolution kinetics of SiO_2 (Gong *et al.*, 2022). Indeed, the conductivity measurements were obtained instantly after the addition of NaOH. The silica dissolution experiment revealed that in addition to silica solubility and speciation, the kinetics of silica solubility should be taken into consideration as well. This may help us to understand which type of phyllosilicate is formed depending on the amount of dissolved silica. In domain 2, due to the small amount of silica dissolved, 1:1-type phyllosilicate phases are formed, whereas in domain 3, 2:1-type phyllosilicate phases, which need more silicon, are formed due to the greater amount of dissolved silica. It should be noted that poorly crystalline 2:1 phyllosilicate-like phase also formed in domain 1 despite there being only a very small amount of dissolved silica.

Discussion

Figure 8 summarizes the mineral phases detected in each domain of pH in the synthesis products.

Although working in air, the results showed that a portion of the Fe ions introduced in the reaction mixture as Fe(II) sulfate stayed as Fe(II) throughout the experiment and was incorporated as such into the neo-formed mineral phases. The presence of hematite in all samples suggested partial oxidation of Fe(II) to
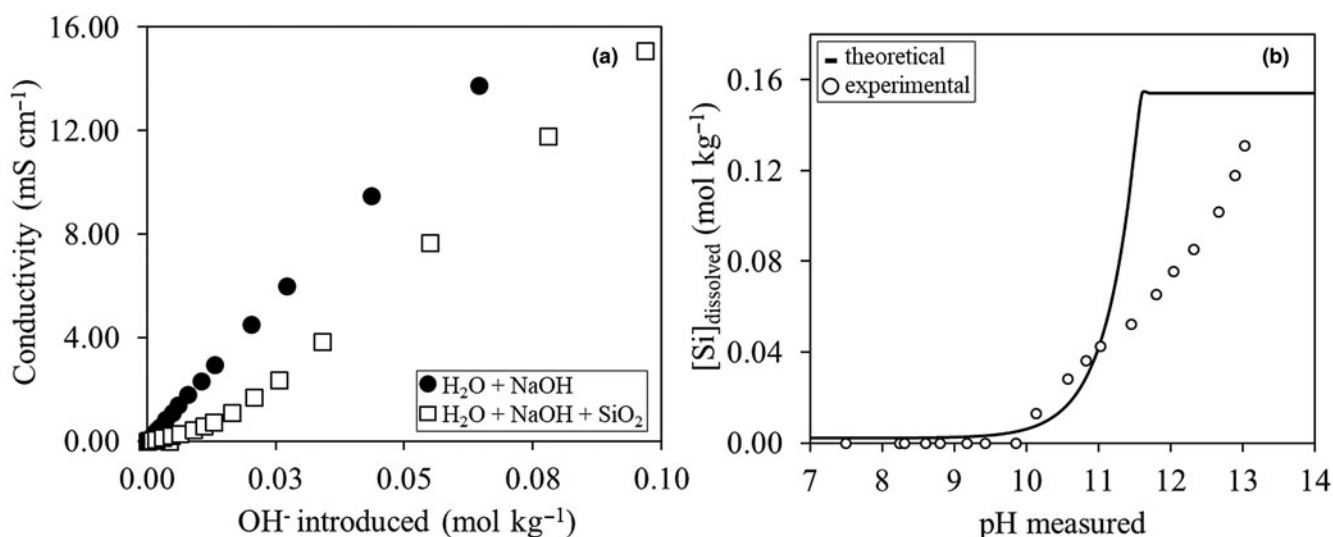
Figure 7. (a) Solution conductivity as a function of the amount of OH^- introduced and (b) a comparison between the theoretical and calculated solubility of silica as a function of pH at 298 K.

Domain 1 $pH_i < 9.67$	Magnetite, SiO$_2$
	Goethite
	Hematite
	Fe^{III} 2:1 clay mineral
Domain 2 $9.67 \leq pH_i \leq 10.75$	Hematite
	Fe^{III}/Fe^{II} 1:1 clay mineral
Domain 3 $pH_i > 10.75$	Hematite
	Fe^{III}/Fe^{II} 1:1 clay mineral
	Fe^{III}/Fe^{II} 2:1 clay mineral

Figure 8. Summary of characteristic mineral phases identified in each pH domain.

Fe(III). Various reaction pathways can lead to the formation of hematite (Schwertmann & Cornell, 2000). It could have formed from goethite during the hydrothermal treatment or precipitated during the hydrolysis and condensation reactions from Fe(III)-containing solutions during the ageing of the precursor (cf. Supplementary Material, reactions 2 and 3) or by oxidation of magnetite. The presence of hematite thus indicates that a portion of the Fe(II) initially introduced in the reaction mixture underwent oxidation, but this could have happened at different times.

The formation of phyllosilicate-like compounds occurred across the range of pH values tested, but their crystallinity and type might be correlated with the solubility and speciation of silica, which in turn is governed by the pH of the solution. At acidic pH and in a weakly basic solution below pH 9, the solubility of silica is very low, the main species in solution is H$_4$SiO$_4$ and poorly crystalline Fe^{III}-bearing 2:1-type phyllosilicate was identified. A possible precipitation equation is given in the Supplementary Material (reaction 4). This finding is in agreement with previous studies regarding glass corrosion, in which a 2:1-type phyllosilicate phase (nontronite-like) and/or iron oxides were identified (Carriere *et al.*, 2021; Kikuchi *et al.*, 2022; Galai *et al.*, 2023). It is important to note that the 2:1-type phyllosilicate-like phase was poorly crystallized and can be considered amorphous (Fig. S1). It could be easily overlooked if the sample is studied using the more common characterization techniques such as XRD with a copper lamp. In our case, we used high-resolution energy-dispersive 1-D detector equipment for XRD to reduce the iron fluorescence contribution from the sample. However, the presence of this phase could be an important indicator of ongoing glass corrosion, or it might be present in the silica-rich solution-conducting pipes.

Above pH 9, the solubility of silica increases and highly crystalline phyllosilicate-like phases were obtained. The type of phase could be correlated with the amount of dissolved silica available and its speciation. The formation of a 1:1-type phyllosilicate-like phase coincided with the presence of H$_3$SiO$_4^-$ species in solutions above pH 9.5 and with low amounts of H$_4$SiO$_4$. A possible precipitation equation is given in the Supplementary Material (reaction 5). Previous studies (Pignatelli *et al.*, 2014; Tosca *et al.*, 2016; Hinz *et al.*, 2021) have also reported the formation of serpentine-like phases at approximately this pH, albeit slightly closer to neutral pH (i.e. pH 7–8).

At a basic pH > 11, silica is found in a soluble species form mainly as H$_3$SiO$_4^-$ and in a low amount as H$_2$SiO$_4^{2-}$. It should be noted that, in our experiment, some of Aerosil might not have dissolved completely. Indeed, conductimetry measurements

showed that more than 6 h would be needed to solubilize entirely the initially introduced amount of silica. However, when more significant amounts of silicon are present in solution in soluble form, both types of phyllosilicates were observed to form: Fe^{III}/Fe^{II}-bearing 1:1-type phyllosilicate and Fe^{III}/Fe^{II}-bearing 2:1-type phyllosilicate. Possible precipitation equations are given in the Supplementary Material (reactions 6 and 7). The Mössbauer spectroscopy results differentiated between the Fe(II) and Fe(III) components, and two Fe(II) components were identified. However, the question remains as to which component would belong to the 1:1-type phase and which to the 2:1-type phase. Although distinguishing between iron oxides (magnetically ordered) and phyllosilicates (paramagnetic) is straightforward at low temperatures, the fact remains that mixtures of phyllosilicates are prone to complicating their respective identification on the basis of their paramagnetic components alone and their oxidation state or Fe atomic environmental information (i.e. centre shift and quadrupole splitting). Consequently, structural characterization tools (XRD, TEM) remain essential if samples are not affected by crystallinity problems. The best situation is to complement the results from Mössbauer spectroscopy with these mineralogical structural methods.

In the precipitation reactions given in the Supplementary Material, we had assumed that iron was in the form of Fe^{2+} in solution (we used FeSO$_4\cdot$7H$_2$O as an iron source), but it is very likely that some of iron was actually in the form of Fe^{3+}. Indeed, the study of Hinz *et al.* (2021) indicates that the presence of Fe^{3+} is necessary to trigger the precipitation of greenalite (1:1-type phyllosilicate belonging to the serpentine group). The repartition between Fe^{2+} and Fe^{3+} in the precursor solution would govern the necessity of adding O$_2$ to the reactants or H$_2$ to the products to establish truly representative precipitation reactions. In summary, precise knowledge of the amount of Fe^{2+} and Fe^{3+} in the precursor solution would allow us to establish precipitation equations and provide information regarding the possible formation conditions of such phases.

Conclusion

The influence of pH on the hydrothermal synthesis of iron-rich phyllosilicates was investigated in this study. The findings indicate that pH governed the crystallinity and nature of the obtained phyllosilicate-like phases. Three domains of pH were identified, and these were correlated with silica availability and speciation in the solution: domain 1 with pH_i < 9.67, domain 2 with 9.67 < pH_i < 10.75 and domain 3 with pH_i > 10.75. The formation of 1:1-type iron-rich phyllosilicate coincided with the low presence of H$_3$SiO$_4^-$ aqueous species at pH > 9.5. For higher pH values and higher amounts of H$_3$SiO$_4^-$ aqueous species, both 1:1-type and 2:1-type iron-rich phyllosilicates were found. In future, precise knowledge of the quantity of Si, Fe^{2+} and Fe^{3+} in the solution at every stage of such processes as those investigated here would allow for a better understanding of phyllosilicate-like phase precipitation mechanisms.

Conflicts of interest. The authors declare none.

References

Alexander G.B., Heston W.M. & Iler R.K. (1954) The solubility of amorphous silica in water. *Journal of Physical Chemistry*, **58**, 453–455.

Baron F., Petit S., Tertre E. & Decarreau A. (2016) Influence of aqueous Si and Fe speciation on tetrahedral Fe(III) substitutions in nontronites: a clay synthesis approach. *Clays and Clay Minerals*, **64**, 230–244.

Benali O., Abdelmoula M., Refait P. & Génin J.-M.R. (2001) Effect of orthophosphate on the oxidation products of Fe(II)–Fe(III) hydroxycarbonate: the transformation of green rust to ferrihydrite. *Geochimica et Cosmochimica Acta*, **65**, 1715–1726.

Bertoldi, C., Dachs, E., Cemic, L., Theye, T., Wirth, R. & Groger, W. (2005) The heat capacity of the serpentine subgroup mineral berthierine $(Fe_{2.5}Al_{0.5})[Si_{1.5}Al_{0.5}O_5](OH)_4$. *Clays and Clay Minerals*, **53**, 380–388.

Boumaiza H., Dutournié P., Le Meins J.-M., Limousy L., Brendlé J., Martin C. et al. (2020) Iron-rich clay mineral synthesis using design of experiments approach. *Applied Clay Science*, **199**, 105876.

Carriere C., Neff D., Martin C., Tocino F., Delanoë A., Gin S. et al. (2021) AVM nuclear glass/steel/claystone system altered by Callovo–Oxfordian poral water with and without cement–bentonite grout at 70°C. *Materials and Corrosion*, **72**, 474–482.

Criouet I., Viennet J.C., Baron F., Balan E., Buch A., Delbes L. et al. (2023) Influence of pH on the hydrothermal Ssynthesis of Al-substituted smectites (saponite, beidellite, and nontronite). *Clays and Clay Minerals*, **71**, 539–558.

Cundy C.S. & Cox P.A. (2005) The hydrothermal synthesis of zeolites: precursors, intermediates and reaction mechanism. *Microporous and Mesoporous Materials*, **82**, 1–78.

de Faria D.L.A., Venâncio Silva S. & de Oliveira M.T. (1997) Raman microspectroscopy of some iron oxides and oxyhydroxides. *Journal of Raman Spectroscopy*, **28**, 873–878.

de Kimpe C., Gastuche M.C. & Brindley G. (1961) Ionic coordination in alumino-silicic gels in relation to clay mineral formation. *American Mineralogist*, **46**, 1370–1381.

Decarreau A. & Bonnin D. (1986) Synthesis and crystallogenesis at low temperature of Fe(III)-smectites by evolution of coprecipitated gels: experiments in partially reducing conditions. *Clay Minerals*, **21**, 861–877.

Doelsch E., Rose J., Masion A., Bottero J.Y., Nahon D. & Bertsch P.M. (2002) Hydrolysis of Iron(II) Chloride under anoxic conditions and influence of SiO_4 ligands. *Langmuir*, **18**, 4292–4299.

Dyar M.D., Agresti D.G., Schaefer M.W., Grant C.A. & Sklute E.C. (2006) Mössbauer spectroscopy of Earth and planetary materials. *Annual Review of Earth and Planetary Sciences*, **34**, 83–125.

Dzene L., Brendlé J., Limousy L., Dutournié P., Martin C. & Michau N. (2018) Synthesis of iron-rich tri-octahedral clay minerals: a review. *Applied Clay Science*, **166**, 276–287.

Eikenberg J. (1990) *On the Problem of Silica Solubility at High pH*. Paul Scherrer Institut, Würenlingcn und Villigen, Switzerland, 59 pp.

Felmy A.R., Cho H., Rustad J.R. & Mason M.J. (2001) An aqueous thermodynamic model for polymerized silica species to high ionic strength. *Journal of Solution Chemistry*, **30**, 509–525.

Francisco P.C.M., Mitsui S., Ishidera T., Tachi Y., Doi R. & Shiwaku H. (2020) Interaction of FeII and Si under anoxic and reducing conditions: structural characteristics of ferrous silicate co-precipitates. *Geochimica et Cosmochimica Acta*, **270**, 1–20.

Frank-Kamenetzkij V.A., Kotov N.V. & Tomashenko A.N. (1973) The role of Al^{IV} and Al^{VI} in transformation and synthesis of layer silicates. *Kristall und Technik*, **8**, 425–435.

Galai L., Marchetti L., Miserque F., Frugier P., Godon N., Brackx E. et al. (2023) Effect of dissolved Si on the corrosion of iron in deaerated and slightly alkaline solutions (pH $\approx$ 8.1) at 50 °C. *Corrosion Science*, **210**, 110790.

Gong K., Aytas T., Zhang S.Y. & Olivetti E.A. (2022) Data-driven prediction of quartz dissolution rates at near-neutral and alkaline environments. *Frontiers in Materials*, **9**, 1–15.

Grubb P.L.C. (1971) Silicates and their paragenesis in the Brockman iron formation of Wittenoom Gorge, Western Australia. *Economic Geology*, **66**, 281–292.

Gunnarsson I. & Arnórsson S. (2000) Amorphous silica solubility and the thermodynamic properties of $H_4SiO°_4$ in the range of 0° to 350°C at P_{sat}. *Geochimica et Cosmochimica Acta*, **64**, 2295–2307.

Halevy I., Alesker M., Schuster E.M., Popovitz-Biro R. & Feldman Y. (2017) A key role for green rust in the Precambrian oceans and the genesis of iron formations. *Nature Geoscience*, **10**, 135–139.

Harder H. (1978) Synthesis of iron layer silicate minerals. *Clays and Clay Minerals*, **26**, 65–72.

Herbert H.-J., Kasbohm J., Nguyen-Thanh L., Meyer L., Hoang-Minh T. et al. (2016) Alteration of expandable clays by reaction with iron while being percolated by high brine solutions. *Applied Clay Science*, **121–122**, 174–187.

Hinz I.L., Nims C., Theuer S., Templeton A.S. & Johnson J.E. (2021) Ferric iron triggers greenalite formation in simulated Archean seawater. *Geology*, **49**, 905–910.

Jaber M., Komarneni S. & Zhou C.-H. (2013) Synthesis of clay minerals. Pp. 223–241 in: *Handbook of Clay Science Fundamentals* (F. Bergaya & G. Lagaly, editors). Elsevier, Amsterdam, The Netherlands.

Kikuchi R., Sato T., Fujii N., Shimbashi M. & Arcilla C.A. (2022) Natural glass alteration under a hyperalkaline condition for about 4000 years. *Scientific Reports*, **12**, 1–10.

Kilaas R. (1998) Optimal and near-optimal filters in high-resolution electron microscopy. *Journal of Microscopy*, **190**, 45–51.

Kloprogge J.T. (1994) Solid-state nuclear magnetic resonance spectroscopy on synthetic ammonium/aluminum-saponites. *Clays and Clay Minerals*, **42**, 416–420.

Kloprogge J.T. (1998) Synthesis of smectites and porous pillared clay catalysts: a review. *Journal of Porous Materials*, **5**, 5–41.

Konhauser K.O., Amskold L., Lalonde S.V., Posth N.R., Kappler A. & Anbar A. (2007) Decoupling photochemical Fe(II) oxidation from shallow-water BIF deposition. *Earth and Planetary Science Letters*, **258**, 87–100.

Lanson B., Lantenois S., van Aken P.A., Bauer A. & Plancon A. (2012) Experimental investigation of smectite interaction with metal iron at 80 °C: structural characterization of newly formed Fe-rich phyllosilicates. *American Mineralogist*, **97**, 864–871.

Lantenois S., Lanson B., Muller F., Bauer A., Jullien M. & Plançon A. (2005) Experimental study of smectite interaction with metal Fe at low temperature: 1. Smectite destabilization. *Clays and Clay Minerals*, **53**, 597–612.

Manceau A. (1995) Crystal chemistry of hydrous iron silicate scale deposits at the Salton Sea Geothermal Field. *Clays and Clay Minerals*, **43**, 304–317.

Marks L.D. (1996) Wiener-filter enhancement of noisy HREM images. *Ultramicroscopy*, **62**, 43–52.

Meite F., Hauet T., Billard P., Ferté T., Abdelmoula M. & Zegeye A. (2022) Insight into the magnetic properties of Pb-dopped iron oxide nanoparticles during Fe(III) bio-reduction by Shewanella oneidensis MR-1. *Chemical Geology*, **606**, 120904.

Mizutani T., Fukushima Y., Okada A., Kamigaito O. & Kobayashi T. (1991) Synthesis of 1:1 and 2:1 iron phyllosilicates and characterization of their iron state by Mössbauer spectroscopy. *Clays and Clay Minerals*, **39**, 381–386.

Mosser-Ruck R., Cathelineau M., Guillaume D., Charpentier D., Rousset D., Barres O. & Michau N. (2010) Effects of temperature, pH, and iron/clay and liquid/clay ratios on experimental conversion of dioctahedral smectite to berthierine, chlorite, vermiculite, or saponite. *Clays and Clay Minerals*, **58**, 280–291.

Murad E. & Johnston J.H. (1987) Iron oxides and oxyhydroxides. Pp. 507–582 in: *Mössbauer Spectroscopy Applied to Inorganic Chemistry, Volume 2* (G.J. Long, editor). Springer, New York, NY, USA.

Petit S., Baron F. & Decarreau A. (2017) Synthesis of nontronite and other Fe-rich smectites: a critical review. *Clay Minerals*, **52**, 469–483.

Pignatelli I., Bourdelle F., Bartier D., Mosser-Ruck R., Truche L., Mugnaioli E. & Michau N. (2014) Iron–clay interactions: detailed study of the mineralogical transformation of claystone with emphasis on the formation of iron-rich T–O phyllosilicates in a step-by-step cooling experiment from 90 °C to 40 °C. *Chemical Geology*, **387**, 1–11.

Rancourt D.G. & Ping J.Y. (1991) Voigt-based methods for arbitrary-shape static hyperfine parameter distributions in Mössbauer spectroscopy. *Nuclear Instruments and Methods in Physics Research Section B: Beam Interactions with Materials and Atoms*, **58**, 85–97.

Schwertmann U. & Cornell R.M. (editors) (2000) *Iron Oxides in the Laboratory.* Wiley-VCH Verlag GmbH, Weinheim, Germany, 188 pp.

Schwertmann U. & Thalmann H. (1976) The influence of [Fe(II)], [Si], and pH on the formation of lepidocrocite and ferrihydrite during oxidation of aqueous $FeCl_2$ solutions. *Clay Minerals*, **11**, 189–200.

Stucki J.W., Goodman B.A. & Schwertmann U. (editors) (1989) *Iron in Soils and Clay Minerals.* D. Reidel Publishing Company, Dordrecht, The Netherlands, 310 pp.

Tosca N.J., Guggenheim S. & Pufahl P.K. (2016) An authigenic origin for Precambrian greenalite: implications for iron formation and the chemistry of ancient seawater. *Geological Society of America Bulletin*, **128**, 511–530.

Vandenberghe R.E., Barrero C.A., da Costa G.M., Van San E. & De Grave E. (2000) Mössbauer characterization of iron oxides and (oxy)hydroxides: the present state of the art. *Hyperfine Interactions*, **126**, 247–259.